catalysts

MDPI

Article

EPR Investigations of G-C_3N_4/TiO_2 Nanocomposites

Dana Dvoranová [1], Milan Mazúr [1], Ilias Papailias [2], Tatiana Giannakopoulou [2], Christos Trapalis [2] and Vlasta Brezová [1,*]

1 Institute of Physical Chemistry and Chemical Physics, Faculty of Chemical and Food Technology, Slovak University of Technology in Bratislava, Radlinského 9, SK-812 37 Bratislava, Slovakia; dana.dvoranova@stuba.sk (D.D.); milan.mazur@stuba.sk (M.M.)

2 Institute of Nanoscience and Nanotechnology, National Center for Scientific Research "Demokritos", 153 43 Agia Paraskevi, Attikis, Greece; i.papailias@inn.demokritos.gr (I.P.); t.giannakopoulou@inn.demokritos.gr (T.G.); c.trapalis@inn.demokritos.gr (C.T.)

* Correspondence: vlasta.brezova@stuba.sk; Tel.: +421-2-5932-5666

Received: 31 December 2017; Accepted: 23 January 2018; Published: 26 January 2018

Abstract: The g-C_3N_4/TiO_2 nanopowders prepared by the annealing of melamine and TiO_2 P25 at 550 °C were investigated under dark and upon UV or visible-light photoactivation using X- and Q-band electron paramagnetic resonance (EPR) spectroscopy. The EPR spectra of powders monitored at room temperature and 100 K showed the impact of the initial loading ratio of melamine/TiO_2 on the character of paramagnetic centers observed. For the photocatalysts synthesized using a lower titania content, the paramagnetic signals characteristic for the g-C_3N_4/TiO_2 nanocomposites were already found before exposure. The samples annealed using the higher TiO_2 loading revealed the photoinduced generation of paramagnetic nitrogen bulk centers (g-tensor components g_1 = 2.005, g_2 = 2.004, g_3 = 2.003 and hyperfine couplings from the nitrogen A_1 = 0.23 mT, A_2 = 0.44 mT, A_3 = 3.23 mT) typical for N-doped TiO_2. The ability of photocatalysts to generate reactive oxygen species (ROS) upon in situ UV or visible-light photoexcitation was tested in water or dimethyl sulfoxide by EPR spin trapping using 5,5-dimethyl 1-pyrroline N-oxide. The results obtained reflect the differences in photocatalyst nanostructures caused by the differing initial ratio of melamine/TiO_2; the photocatalyst prepared by the high-temperature treatment of melamine/TiO_2 wt. ratio of 1:3 revealed an adequate photoactivity in both spectral regions.

Keywords: g-C_3N_4/TiO_2; EPR spectroscopy; photoinduced processes

1. Introduction

Among the previously-studied potential photocatalysts, TiO_2 polymorphs meet the criteria for large-scale applications. Stability, low cost, relatively low toxicity, and suitable photocatalytic activity predispose TiO_2 to applications in various areas (gas sensors, photocatalysts, solar cells, etc.) [1–4]. However, TiO_2 has several limitations as a photocatalyst; the rapid recombination of photogenerated holes and electrons in the nanosecond scale inhibits the required consecutive reactions of the charge carriers on surface. In addition, the anatase energy band gap E_{bg} ~3.2 eV corresponds to UV light, which rules out visible (VIS) light photoexcitation [5–8]. The attempts to overcome these limits are concentrated mainly on the preparation of new types of TiO_2 nanostructures by controlling the morphology of pristine TiO_2, by non-metal and metal doping or surface modification using noble metals [9–11]. The doping of TiO_2 with metal ions can bring a desired decrease in E_{bg}, but a metal ion itself may serve as an additional recombination center of the charge carriers, resulting in suppressed redox processes on the surface [12]. Concerning the non-metal element doped titania photocatalysts, the modification of TiO_2 nanostructures using a nitrogen dopant represents a promising method to shift photoactivity to the visible region, as shown in numerous previous studies [13–15].

In addition to the intensively investigated metal oxide photocatalysts, recent attention has also been targeted on metal-free semiconducting materials [16,17]. Graphitic carbon nitride (g-C_3N_4) represents a polymeric compound consisting of carbon and nitrogen atoms connected via tri-*s*-triazine-based patterns with some hydrogen impurity. Although the photocatalytic properties of g-C_3N_4 were discovered only in the last decade, this material is regarded as one of the oldest synthetic polymers prepared independently by Berzelius, Liebig, and Gmelin [18]. The energy band gap of graphitic carbon nitride is about 2.7 eV (460 nm) with suitable electronic band structure (conduction band and valence band edge positions at approx. −1.1 V and +1.6 V vs. normal hydrogen electrode (NHE), respectively), predisposing g-C_3N_4 as a promising visible-light active photocatalyst for a variety of applications; e.g., water splitting, NO_x decomposition, or solar energy converting systems (photoelectrochemical cells) [16,17]. The semiconducting g-C_3N_4 reveals high thermal stability and chemical resistance due to the strong covalent bond between C and N atoms. Although the energy band gap of g-C_3N_4 enables VIS-light absorption, its photocatalytic activity is negatively affected by the limited surface area and rapid recombination processes of photogenerated charge carriers [16,19]. The efficiency of photoinduced reactions in the presence of semiconducting photocatalysts is determined by the light absorption coupled with the effective generation of charge carriers, their recombination processes, as well as suitable structure with the surface active sites enabling substrate adsorption [14]. Consequently, the combination of g-C_3N_4 with TiO_2 can merge the benefits of both materials, obtaining a composite photocatalyst with suitable morphological properties and enhanced visible-light activity. The preparation method strongly influences the morphology of g-C_3N_4 nanostructures, as well as their photocatalytic activity [20–23].

Recently, a series of g-C_3N_4/TiO_2 photocatalysts was synthesized via the annealing of melamine and P25 titanium dioxide powders in order to prepare active VIS-light photocatalysts for NO_x removal [24]. The variation in the initial mixture composition allows various semiconducting nanomaterials with E_{bg} in the range of 2.66–3.14 eV to be obtained [24]. In the characterization of photocatalysts, electron paramagnetic resonance (EPR) spectroscopy represents a sensitive tool for the direct detection of paramagnetic defects in solid matrix, as well as for the identification of non-persistent paramagnetic intermediates via indirect methods (e.g., spin trapping technique) [25–27]. Consequently, the aim of our EPR study is to bring insight into the presence of trapped paramagnetic charge carriers or free radicals generated upon UV or VIS-light irradiation in g-C_3N_4/TiO_2 nanopowders or dispersed systems in water or dimethyl sulfoxide (DMSO).

2. Results and Discussion

Organic elemental (CHNS) analysis was performed to obtain information on the nitrogen and carbon content in the annealed photocatalysts. The results, including the sample nomination and the initial melamine/TiO_2 weight ratios, are presented in Table 1.

Table 1. Sample nomination, melamine/TiO_2 weight (wt.) ratio, results of CHNS analysis, and E_{bg} values of the photocatalysts investigated. g-C_3N_4: graphitic carbon nitride.

Sample	Melamine/TiO_2 wt. Ratio	CHNS Content, wt. %			E_{bg}, eV [2]
		C	H	N	
g-C_3N_4	-	34.4	1.78	65.9	2.66
M1	3:1	17.7	1.40	32.1	2.66
M2	1:1	4.41	0.62	6.16	2.74
M3	2:3	1.64	0.44	1.68	2.88
M4	1:3	0.44	0.31	0 [1]	3.00
M5	1:4	0.31	0.33	0 [1]	3.14
M6	1:7	0.13	0.13	0 [1]	3.14

[1] Below detection limit; [2] Ref. [24].

The decreased initial melamine loading corresponds to the drop in N-content, and for photocatalysts M4–M6, the nitrogen concentration was already bellow the detection limit. This finding correlates well with the increase of energy band gap from 2.66 eV established for sample M1 (highest melamine/TiO_2 ratio) up to 3.14 eV found for photocatalysts M5 and M6 (Table 1), matching the E_{bg} value of P25, which represents mixed-phase TiO_2 [24,28,29]. The presence of hydrogen detected in the range 1.78–0.13 wt. % can be attributed to the residual amino groups or to the water adsorbed on the photocatalyst surface, which is in agreement with the recently published IR spectra of the studied photocatalysts [24].

X- and Q-band EPR spectra of the nanocrystalline samples g-C_3N_4 and M1–M6 bring information on the paramagnetic species originating from synthesis, as well as those generated upon in situ photoexcitation with UV or VIS light. Figure 1 illustrates the X- and Q-band EPR spectra of pristine g-C_3N_4 and M1 powder (initial melamine/TiO_2 wt. ratio 3:1) measured in the dark at room temperature (RT) and at 100 K. In the EPR spectra of pristine g-C_3N_4, only a nearly isotropic signal at g = 2.003 (*) was detected (Figure 1), often observed in the EPR spectra of graphitic carbon nitride and attributed to the conduction electrons in the localized π-states of g-C_3N_4 [30]. An analogous EPR signal found in the TiO_2 matrix upon high-temperature treatment was assigned to the medium-polarized conduction electrons or oxygen vacancies [31,32]. Consequently, these electron excess centers may be simultaneously generated during the synthesis of g-C_3N_4/TiO_2 photocatalysts at 550 °C (Figure 1).

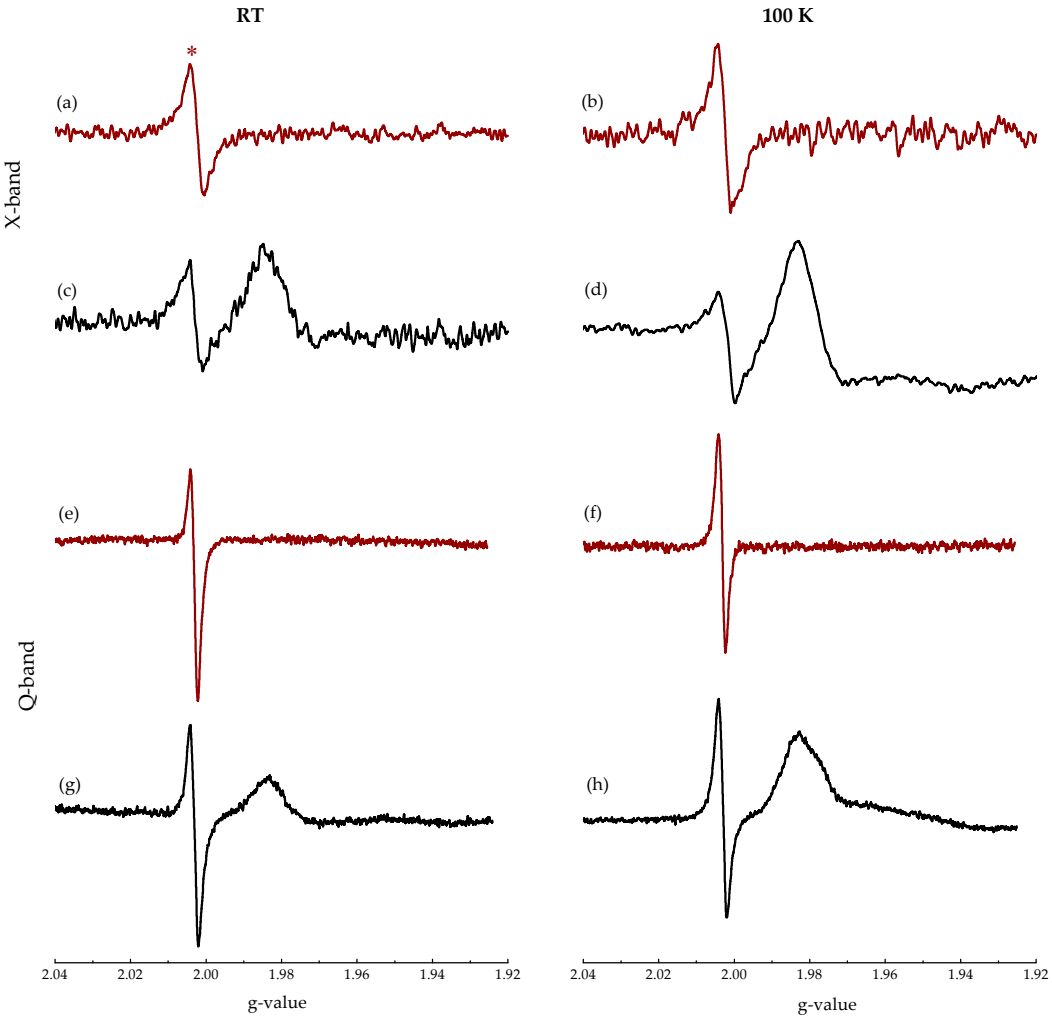

Figure 1. X-band and Q-band EPR spectra of (**a**,**b**,**e**,**f**) pristine g-C_3N_4 powder and (**c**,**d**,**g**,**h**) M1 powder measured in the dark at room temperature (RT) and 100 K. *: Signal at g = 2.003 attributed to the conduction electrons in the localized π-states of g-C_3N_4.

With the aim of obtaining information on the single-line with g = 2.003, the Q-band (~34 GHz) EPR spectra of sample M1 were measured at 100 K using microwave power (P) in the range of 1.4–35.9 mW (data not shown). The linewidth and amplitude dependence on $P^{\frac{1}{2}}$ found for this line (g = 2.003) revealed the spectral changes characteristic for the homogenously broadened line with Lorentzian lineshape observed for EPR lines of systems if the lines are relaxation-determined [33]. Further, the EPR signal with spin-Hamiltonian parameters $g_{\perp}$ = 1.975, $g_{\|}$ = 1.940 observed in the EPR spectra of M1–M6 photocatalysts before exposure unambiguously points to the presence of Ti(III) in rutile allotrope (interstitial sites [32,34,35]), superimposed with a broad line at g ~1.93 attributed to the surface Ti(III) centers in anatase [36]. The short spin-lattice relaxation time of Ti(III) species generally hinders their detection at RT [37]. The Ti(III) ions detectable even in the room temperature X- and Q-band EPR spectra of nanocomposite M1 (Figure 1c,g) are most probably coupled with the oxygen depletion in TiO_2 matrix caused by the high-temperature treatment of melamine/TiO_2 mixture. X- and Q-band EPR spectra of M1 measured at 100 K were fully compatible with the RT spectra, revealing only the increased intensity of Ti(III) signals due to the temperature lowering (Figure 1d,h); no further EPR signals were detected. The EPR signals of Ti(III) with $g_{\perp}$ = 1.975, $g_{\|}$ = 1.940 along with a broad line at g < 1.94 were found in the M2 sample containing the initial melamine/TiO_2 wt. ratio 1:1; however, for samples M3–M6, only the broad line (g < 1.94) was present.

X-band EPR spectra of samples M1–M6 measured at 100 K in the dark and upon visible-light exposure are summarized in Figure 2. A sharp single-line (g = 2.003) was found in the EPR spectra before exposure for all the studied photocatalysts, and it is most probably coupled with the presence of electron excess centers generated during synthesis at 550 °C.

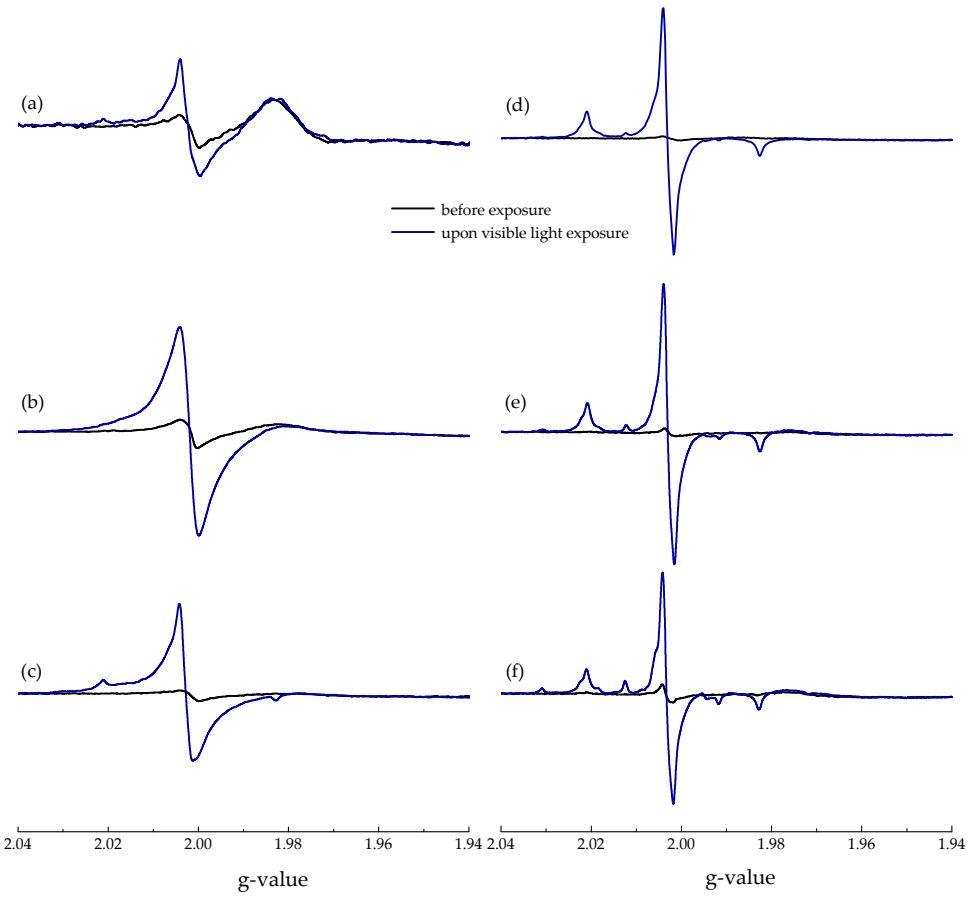

Figure 2. X-band EPR spectra obtained before and upon visible (VIS)-light exposure (160 klx) of nanocrystalline photocatalysts: (**a**) M1; (**b**) M2; (**c**) M3; (**d**) M4; (**e**) M5; and (**f**) M6 at 100 K.

VIS-light exposure had only a negligible effect on the paramagnetic signals of Ti(III) species under the given experimental conditions (Figure 2). EPR spectra obtained upon visible-light photoexcitation reflect the differences in the electronic structure of the individual photocatalysts. VIS-light activation of samples M1 and M2 with a high content of g-C_3N_4 led to a significant increase in the intensity of the nearly isotropic signal, with g = 2.003 indicating the generation of photoexcited electrons in the g-C_3N_4 structure upon the absorption of photons. An analogous increase in the intensity of photogenerated conduction electrons was monitored for the illuminated photocatalyst M3, and simultaneously further signal was generated. Based on the g-tensor components g_1 = 2.005, g_2 = 2.004, g_3 = 2.003 and hyperfine couplings from the nitrogen A_1 = 0.23 mT, A_2 = 0.44 mT, A_3 = 3.23 mT, it was assigned to paramagnetic nitrogen bulk centers $N_b^\bullet$, with nitrogen atom bound to the lattice-oxygen ion [38–43]. Figure 3 summarizes the experimental X-band EPR spectra measured at 100 K upon visible-light exposure of M3 and M4 powders along with their simulations evaluated as a superposition of two paramagnetic signals; i.e., single-line (g = 2.003) and nitrogen bulk centers ($N_b^\bullet$, g_1 = 2.005, g_2 = 2.004, g_3 = 2.003; A_1(N) = 0.23 mT, A_2(N) = 0.44 mT, A_3(N) = 3.23 mT), using their relative concentrations of 80% and 20% for M3, and 11% and 89% for M4, respectively.

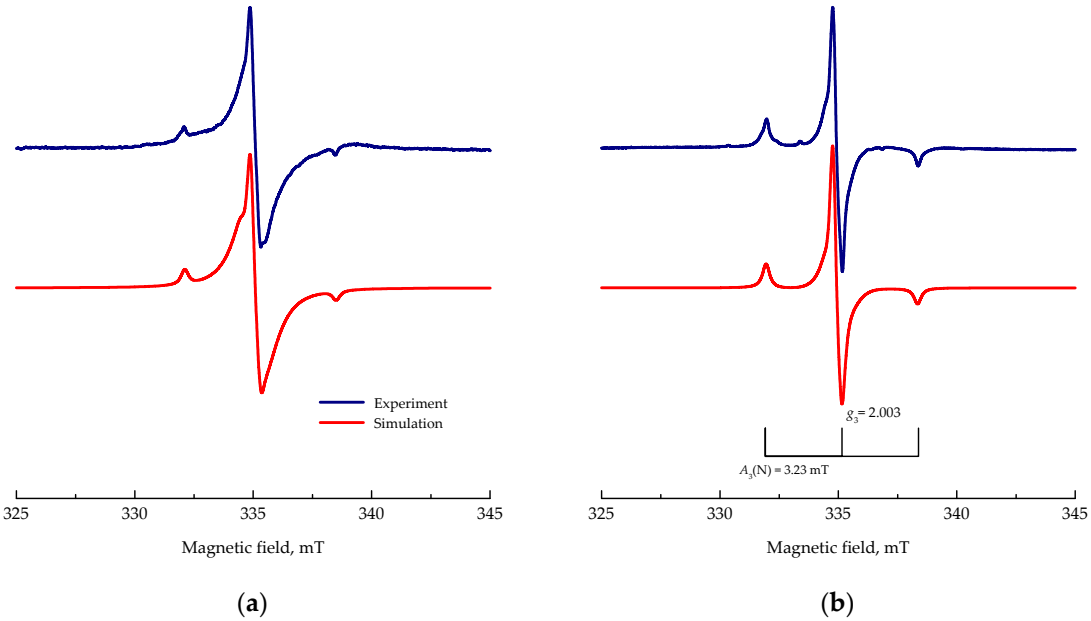

Figure 3. Experimental X-band EPR spectra (blue) measured at 100 K upon visible-light exposure (7-min, 160 klx) of (**a**) M3 and (**b**) M4 powders along with their simulations (red) calculated as superposition of single-line (g = 2.003) and nitrogen bulk centers ($N_b^\bullet$, g_1 = 2.005, g_2 = 2.004, g_3 = 2.003; A_1(N) = 0.23 mT, A_2(N) = 0.44 mT, A_3(N) = 3.23 mT).

The VIS illumination of samples M4–M6 with significantly lowered or not detectable N-content (Table 1) brought further evidence of the generation of EPR signals typical for N-doped TiO_2 photocatalysts. The significant generation of $N_b^\bullet$ upon visible-light exposure of M4–M6 is well compatible with the presence of doubly occupied (diamagnetic N_b^-) centers in the synthesized photocatalysts at the specific lattice positions, and the proper irradiation should promote electrons from these states to the conduction band [38,43]:

$$N_b^- \xrightarrow{h\nu} N_b^\bullet + e^-. \quad (1)$$

The EPR signals of nitric oxide species characterized with spin-Hamiltonian parameters g_1 = 2.001, g_2 = 1.998, g_3 = 1.927; A_1 < 0.1 mT, A_2 = 3.22 mT, A_3 = 0.96 mT found also in the N-doped TiO_2 nanostructures were previously described as the product of the complex oxidation process of nitrogen precursors via high-temperature treatment during titania synthesis [39,44]. This signal was not detected

in the EPR spectra of samples M4–M6 in the dark nor upon exposure. However, careful analysis of the spectra revealed more complex hyperfine structure with a coupling constant of about 1.6 mT (Figure 2e,f). Analogous EPR spectra previously found upon VIS-light illumination of modified nanostructured TiO_2 at 10 K were interpreted as a result of the light-induced excitation of organic residuals from the nitrogen precursors forming diverse organic radicals [45].

The irradiation of nanocrystalline photocatalysts at 100 K resulted in the generation of different paramagnetic species (e.g., $N_b^{\bullet}$ or Ti(III) centers), revealing the complex superimposed EPR spectra (Figures 2 and 3). The EPR resonances of Ti(III) are characterized with $g < 2.00$ [32], allowing the evaluation of the integral EPR intensity of Ti(III) centers in the region with $g < 1.99$, as well as of the other paramagnetic species (region with $g > 1.99$) using the experimental spectra obtained upon/before UV or visible-light exposure; their ratio represents the relative EPR integral intensity upon exposure. Figure 4 gathers the results obtained upon UV or visible-light exposure for g-C_3N_4 and M1–M6 photocatalysts. UV or visible-light exposure had a negligible effect on the paramagnetic signals of Ti(III) species under the given experimental conditions, as only a slight decrease of Ti(III) relative integral intensity was detected, most probably due to the electron transfer between $N_b^{\bullet}$ and Ti(III) [43]. The photoexcitation of g-C_3N_4 generated conduction electrons in the localized π-states ($g = 2.003$), with negligible activity upon VIS exposure. The response to visible light regarding the paramagnetic species generation ($g > 1.99$) in samples M1–M6 at 100 K was significantly more intense in comparison to UV exposure, and a significant increase was found for samples M4–M6 with structure representing N-doped TiO_2 (Figure 4). Such behavior is well compatible with the visible-light activation of N_b^{-} species producing paramagnetic $N_b^{\bullet}$ (Equation (1)) [38,43].

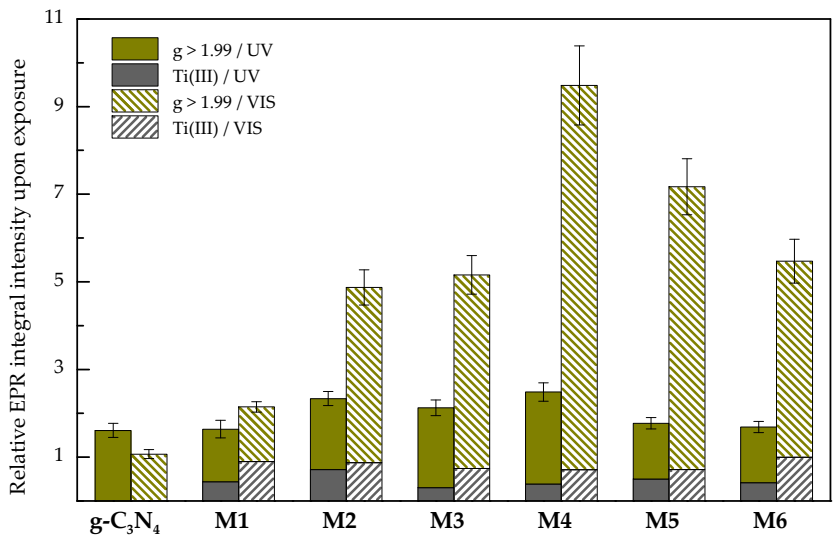

Figure 4. Relative EPR integral intensity upon 7-min VIS-light (160 klx) and UV (λ_{max} = 365 nm; irradiance 20 mW cm^{-2}) exposure, elucidated from X-band EPR spectra of pristine g-C_3N_4 and M1–M6 nanopowders measured at 100 K.

The photoexcitation of photocatalysts dispersed in solvent results in the redox reactions of photogenerated charge carriers on the surface, frequently coupled with the formation of non-persistent radical species. The efficient photocatalytic decomposition of a pollutant in water or in air is often initiated by reactive oxygen species (ROS), especially $^{\bullet}OH$, $O_2^{\bullet-}$, or H_2O_2 generated on the illuminated surface of the photocatalyst [46]. To detect the production of reactive free radicals upon UV or visible-light irradiation, we applied an EPR spin trapping technique using 5,5-dimethyl-pyrroline N-oxide (DMPO) as a spin trapping agent. This approach enables an indirect detection and identification of non-persistent radical intermediates using continuous-wave EPR spectroscopy. The method is based on the reaction of a diamagnetic spin trapping agent with transient radical,

forming more stable paramagnetic spin-adduct. DMPO is the most convenient spin trap applied in photochemical systems due to its low photoactivity, wide potential window, and solubility in polar and non-polar solvents [25,47–49].

The ability of the studied photocatalysts to generate hydroxyl radical upon irradiation was tested in aerated aqueous suspensions in the presence of DMPO. Figure 5 shows that while the UV exposure (λ_{max} = 365 nm, 15 mW cm^{-2}) of aerated aqueous suspensions of M4–M6 led to an immediate increase in the typical four-line signal of •DMPO-OH (spin-Hamiltonian parameters a_N = 1.495 mT, $a_H{}^{\beta}$ = 1.471 mT, g = 2.0057 [50]; inset in Figure 5b), for photocatalysts M1–M3 only a negligible concentration of •DMPO-OH spin-adduct was monitored. To compare the generation of hydroxyl radicals by the individual samples, the concentration of •DMPO-OH spin-adduct upon exposure was evaluated from the double-integrated EPR spectra (Figure 5a). Figure 5b summarizes the •DMPO-OH concentration found for M1–M6 and pristine P25 as a benchmark after 180-s exposure (radiation dose 2.7 J cm^{-2}), evidencing the different behavior for samples M1–M3 (g-C_3N_4/TiO_2 nanocomposites) and M4–M6 (N-doped TiO_2). The results obtained in the EPR spin trapping experiments correlate well with the previously determined valence band edge potentials for the synthesized photocatalysts M1–M6. Only photocatalysts M4–M6 possessed suitable valence band edge positions (2.15–2.46 V vs. NHE) for the generation of hydroxyl radicals [24]. To exclude the alternative mechanisms of •DMPO-OH formation [51], dimethyl sulfoxide as an effective scavenger of hydroxyl radicals [25] was added into the aqueous photocatalyst suspensions. Upon UV exposure of M6/DMPO/H_2O:DMSO (5:1, vol.)/air, the six-line signal of carbon-centered spin-adduct •DMPO-CH_3 (a_N = 1.616 mT, $a_H{}^{\beta}$ = 2.3121 mT, g = 2.0056) dominates the EPR spectrum [50].

The hydroxyl radicals detected in the continuously irradiated photocatalytic systems may be produced via different mechanisms, including also the photocatalytic/photochemical processes of hydrogen peroxide formed during the reduction of dissolved oxygen by the photogenerated electrons in aqueous media [46,52]. Spin trapping experiments in the aqueous suspensions using VIS irradiation (data not shown) confirmed only negligible concentration of •DMPO-OH (comparable with reference experiment), even using the prolonged exposure of M1–M6 without any impact of photocatalysts' structure, in correlation with the limited photolysis of H_2O_2 upon VIS-light exposure.

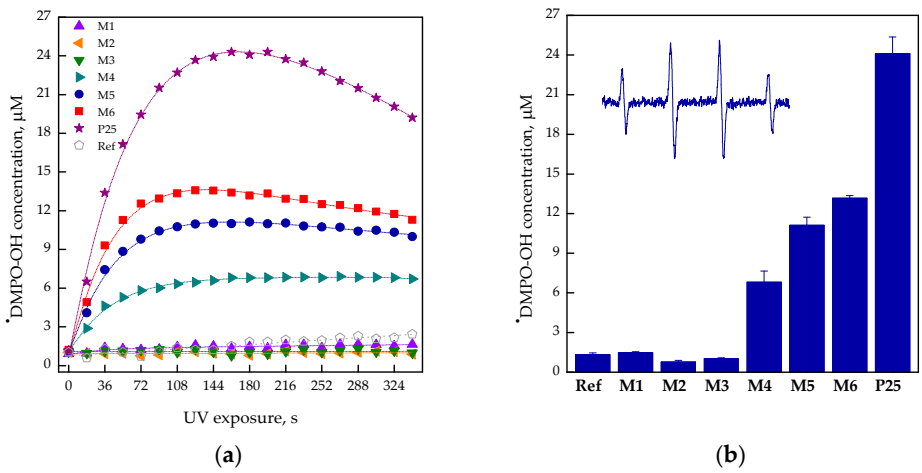

Figure 5. (**a**) Concentration of •DMPO-OH spin-adduct evaluated from double-integrated EPR spectra monitored upon UV exposure (λ_{max} = 365 nm; irradiance 15 mW cm^{-2}) of aerated aqueous suspensions M1–M6 and P25, along with reference (photocatalyst-free solution). (**b**) The concentration of •DMPO-OH spin-adduct determined after 180-s exposure of M1–M6 and P25. The inset in (**b**) represents the EPR spectrum of •DMPO-OH (magnetic field sweep of 6 mT) measured using sample M6. Initial concentrations: c(photocatalyst) = 0.33 g L^{-1}, c_0(DMPO) = 0.035 M. DMPO: 5,5-dimethyl-pyrroline N-oxide.

A suitable position of the conduction band edge towards the one-electron reduction of molecular oxygen ($O_2/O_2^{\bullet-}$) enables the photoinduced generation of superoxide radical anion in the aerated photocatalyst suspensions [24]. As for g-C_3N_4, the position of the conduction band edge was negatively shifted in comparison to titania, enabling the larger thermodynamic potential driving force to the reaction of photogenerated electrons with molecular oxygen producing $O_2^{\bullet-}$; thus, we also expected the formation of DMPO spin-adducts upon visible-light exposure. However, due to the consecutive reactions of $O_2^{\bullet-}$ in aqueous systems [52], its detection via spin trapping using DMPO is not straightforward [53]. Superoxide radical anion is stable when a proton source is absent, and reversible O_2 reduction in several aprotic solvents typically occurs at $E \sim -1.0$ V vs. saturated calomel electrode (SCE) [52]. Consequently, to stabilize the photogenerated superoxide radical anion and its DMPO spin-adduct, the photocatalytic experiments with the photocatalysts M1–M6 were performed in aprotic DMSO. Figure 6 illustrates the experimental and simulated EPR spectrum (including its deconvolution to two individual signals) obtained upon visible exposure of aerated DMPO/DMSO suspension of M5.

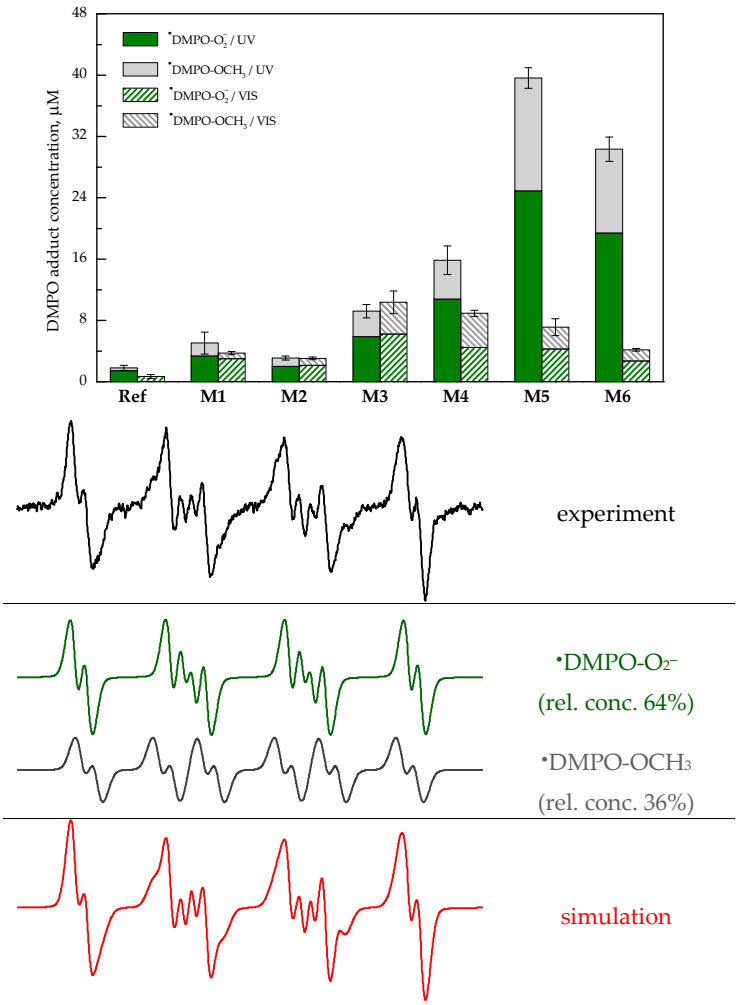

Figure 6. The concentration of DMPO spin-adducts evaluated from the EPR spectra obtained in the aerated DMSO suspension of M1–M6 and P25 photocatalysts, along with reference (photocatalyst-free solution) in the presence of the DMPO spin trap upon 180-s UV exposure (λ_{max} = 365 nm; irradiance 15 mW cm^{-2}) or 480-s visible (160 klx) light. Experimental EPR spectrum (magnetic field sweep of 5 mT) measured in the aerated DMSO suspension of M5 in the presence of DMPO upon VIS-light exposure along with the simulated EPR spectrum obtained by the simulation analysis as a linear combination of two individual spin-adducts $^{\bullet}$DMPO-O_2^- and $^{\bullet}$DMPO-OCH_3. Initial concentrations: c(photocatalyst) = 0.33 g L^{-1}, c_0(DMPO) = 0.035 M.

The twelve-line signal of $^{\bullet}$DMPO-O_2^- characterized with spin-Hamiltonian parameters (a_N = 1.277 mT, $a_H{}^{\beta}$ = 1.033 mT, $a_H{}^{\gamma}$ = 0.138 mT, g = 2.0057) dominates the EPR spectrum, and is superimposed with $^{\bullet}$DMPO-OCH_3 (a_N = 1.310 mT, $a_H{}^{\beta}$ = 0.815 mT, $a_H{}^{\gamma}$ = 0.180 mT, g = 2.0057), which is produced via interaction of solvent with photogenerated ROS [54].

To compare the impact of UV and visible-light exposure, Figure 6 summarizes the concentration of both DMPO spin-adducts found in the irradiated DMSO/DMPO suspensions of photocatalysts M1–M6 and P25 after defined exposure. While comparable concentration of DMPO spin-adducts was found for samples M1–M3 upon UV or visible-light exposure, a significant decrease of spin-adduct concentration upon VIS illumination was monitored for samples M4–M6. Such behavior reflects their increased energy band gaps (Table 1), and is compatible with the previously obtained data upon the visible-light exposure of N-doped TiO_2 nanopowders [55]. However, EPR spectra of M4–M6 nanopowders at 100 K confirm that the visible-light activity was coupled with the photoactivation of N_b^- species, producing paramagnetic nitrogen bulk centers $N_b^{\bullet}$ and electron (Equation (1)), which can be scavenged by the dissolved oxygen, producing $O_2^{\bullet-}$ detected in aprotic DMSO as the corresponding DMPO spin-adduct (Figure 6).

Our previous EPR and UV/VIS experiments evidenced that photoinduced one-electron reduction of 2,2′-azino-bis(3-ethylbenzothiazoline-6-sulfonic acid) diammonium salt $(ABTS)^{\bullet+}$ radical cation to diamagnetic ABTS (standard electrode potential for $ABTS^{\bullet+}$/ABTS is +0.68 V vs. NHE [56]) represents an efficient tool to measure the photoinduced activity of the photocatalysts in the dispersed systems, as $ABTS^{\bullet+}$ radical cation can be reduced by photogenerated electrons as well as $O_2^{\bullet-}$ [26,51]. This process can be followed by EPR spectroscopy, monitoring the changes in the intensity of an overmodulated EPR signal of $ABTS^{\bullet+}$ (g = 2.0036; inset in Figure 7b).

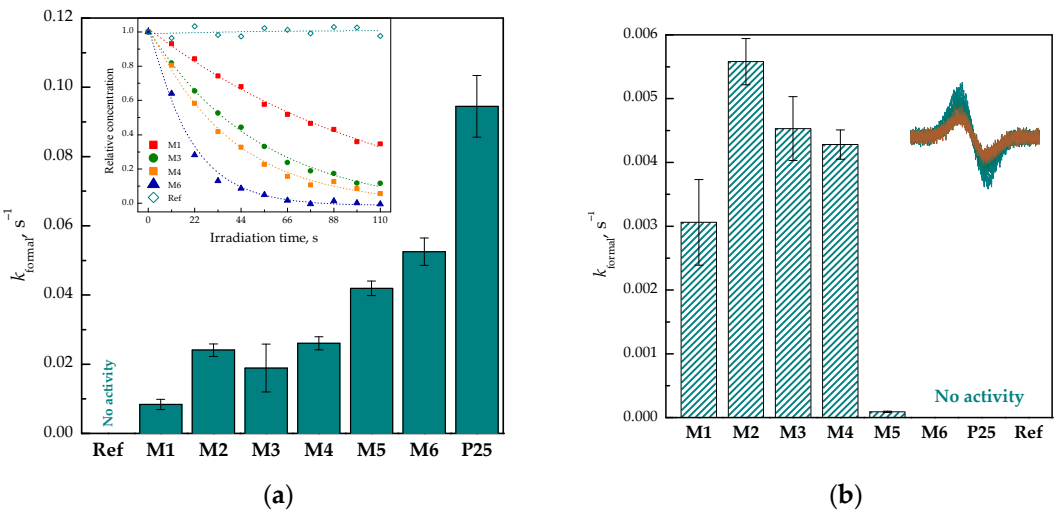

Figure 7. Formal rate constants of 2,2′-azino-bis(3-ethylbenzothiazoline-6-sulfonic acid) diammonium salt $(ABTS)^{\bullet+}$ radical cation reduction in the presence of photocatalysts M1–M6 and P25, along with reference (photocatalyst-free solution) upon continuous (**a**) UV (λ_{max} = 365 nm; 15 mW cm^{-2}) or (**b**) VIS-light (160 klx) irradiation evaluated from the EPR spectra. Initial concentrations: c(photocatalyst) = 0.33 g L^{-1}; $c_0(ABTS^{\bullet+})$ = 43 μM. Inset in (**a**): Dependence of the $ABTS^{\bullet+}$ relative concentration on the irradiation time measured under analogous conditions. Inset in (**b**): Intensity decline in EPR spectra (magnetic field sweep of 6 mT, modulation amplitude of 0.2 mT) of $ABTS^{\bullet+}$ measured in the aerated aqueous M3 suspension monitored in 60-s intervals during 600-s VIS-light exposure.

The aerated aqueous solutions of $ABTS^{\bullet+}$ revealed the sufficient stability upon UV or visible-light exposure, which is a key point in the application in the irradiated photocatalytic systems (Figure 7a). The decline of $ABTS^{\bullet+}$ in aqueous aerated suspensions containing photocatalysts M1–M6 and P25 was measured in situ either during a 100-s UV exposure (λ_{max} = 365 nm, 15 mW cm^{-2}) or during a

600-s visible-light exposure (160 klx). From the individual EPR spectra, the integral EPR intensity related to $ABTS^{\bullet+}$ concentration was evaluated and the changes of $ABTS^{\bullet+}$ relative concentration upon exposure were described by the formal first-order kinetic model (inset in Figure 7a). The calculated formal rate constants were used to compare the efficiency of $ABTS^{\bullet+}$ photoreduction in the presence of photocatalysts, as is shown in Figure 7 for photocatalysts M1–M6 and P25. Upon UV exposure, the $ABTS^{\bullet+}$ photoreduction formal rate constant increased with the enhanced content of titania in photocatalysts, and the UV-induced redox activity of samples M1–M6 was well compatible with results of spin trapping experiments in water or DMSO (Figures 5b and 6). The visible-light-induced reduction of $ABTS^{\bullet+}$ was evidenced only for samples M1–M4 with the suitable values of band gap energy (formal rate constant about ten-times lower) [24]. Considering the role of N_b^- species in the visible-light activation of photocatalysts M4–M6 coupled with generation of electrons suitable for the reduction of molecular oxygen evidenced in aprotic solvent (Figure 6), most probably such redox processes of $ABTS^{\bullet+}$ are limited in aqueous suspensions.

3. Materials and Methods

Composite g-C_3N_4/TiO_2 materials were prepared by annealing melamine (Fluka, Buchs, Switzerland) and dry mixtures of melamine and commercial TiO_2 Aeroxide® P25 (Evonik Degussa, Essen, Germany), as is described in [24]. The stock suspensions containing M1–M6 or P25 of 1 mg mL^{-1} were prepared in redistilled water or dimethyl sulfoxide (DMSO; SeccoSolv® Merck, Darmstadt, Germany). 2,2′-Azino-bis(3-ethylbenzothiazoline-6-sulfonic acid) diammonium salt (ABTS), potassium persulfate, and 4-hydroxy-2,2,6,6-tetramethylpiperidine N-oxyl (TEMPOL) obtained from Sigma-Aldrich (Buchs, Switzerland) were used as supplied. The spin trapping agent 5,5-dimethyl-1-pyrroline N-oxide (DMPO; Sigma-Aldrich, Buchs, Switzerland) was distilled prior to the application. The ABTS molecule was oxidized by $K_2S_2O_8$ to the corresponding radical cation ($ABTS^{\bullet+}$) according to the previously reported procedure [51], and the precise concentration of $ABTS^{\bullet+}$ was determined by UV/VIS spectroscopy ($\varepsilon_{735\,nm}$ = 1.5 × 10^4 M^{-1} cm^{-1}) [57] using a UV-VIS-NIR spectrophotometer Shimadzu UV3600 (Kyoto, Japan).

The EPR experiments of powders at room temperature (RT) and at low temperature (100 K) were performed by EMX Plus EPR spectrometer (Bruker, Rheinstetten, Germany) operating in Q-band in the standard ER 5106 QT Q-band probe for cw-EPR and by EMX EPR spectrometer (Bruker, Rheinstetten, Germany) operating in X-band at 100 kHz field modulation in the standard TE_{102} (ER 4102 ST) rectangular cavity using thin-walled quartz EPR tubes (Bruker). The temperature was lowered to 100 K by the temperature control unit ER 4141VT-U (Q-band; Bruker) or ER 4111 VT (X-band; Bruker), with liquid nitrogen as the refrigerant. The *g*-values were determined with an uncertainty of ±0.0005 by the simultaneous measurement of a reference sample containing Mn(II)/MgO standard or standard strong pitch (Bruker) placed on the wall of the EPR cell or using a nuclear magnetic resonance teslameter (ER 036TM, Bruker) and integrated frequency counter. The experimental solid state EPR spectra were analyzed by the Bruker software WinEPR, and the simulated spectra were calculated with the EasySpin toolbox [58]. The EPR spectra of powder TiO_2 samples were recorded at RT or at 100 K, in dark or upon continuous in situ UV (λ_{max} = 365 nm; Bluepoint LED, Hönle UV Technology, Gräfelfing/München, Germany) or visible light (KL 1600LED (T = 5600 K; Schott, Mainz, Germany) photoexcitation. The value of illuminance for visible light was measured by a digital lux meter (Metra, Blansko, Czech Republic).

The generation/reduction of paramagnetic species upon UV and visible-light exposure of samples M1–M6 and P25 in suspensions was monitored by cw-EPR spectroscopy using the EMX plus X-band EPR spectrometer. The detailed procedure is described in [25–27]. All of the EPR experiments were carried out at least in triplicate. The concentration of photogenerated spin-adducts was evaluated from the double-integrated EPR spectra based on the calibration curve obtained from the EPR spectra of TEMPOL solutions measured under strictly identical experimental conditions. The experimental isotropic EPR spectra were simulated using Winsim2002 software (NIEHS, Durham, NC, USA) suitable

for analysis and fitting of multi-component isotropic EPR spectra of nitroxide radicals [59]. The g-values of spin-adducts were determined with an uncertainty of ±0.0001 using a nuclear magnetic resonance teslameter and integrated frequency counter.

The CHNS analyses were performed on EA CHNS(O) Flash 1112 (Thermo Finnigan, San Jose, CA, USA).

4. Conclusions

The paramagnetic centers of pristine g-C_3N_4 and g-C_3N_4/TiO_2 nanopowders prepared by the annealing of various ratios of dry melamine and TiO_2 P25 at 550 °C were investigated using EPR spectroscopy in the dark, as well as upon UV and visible-light photoactivation. Before exposure, the X- and Q-band EPR spectra of samples M1–M6 correspond to the signal of the conduction electrons in the localized π-states in g-C_3N_4 or oxygen vacancies in TiO_2 matrix (g = 2.003) along with resonances typical for various Ti(III) centers. The visible-light photoexcitation of g-C_3N_4 and M1–M3 photocatalysts resulted in the predominant generation of a single-line EPR signal of the conduction electrons in the localized π-states in g-C_3N_4 and the spectrum of nitrogen bulk centers $N_b^{\bullet}$ (g_1 = 2.005, g_2 = 2.004, g_3 = 2.003; A_1(N) = 0.23 mT, A_2(N) = 0.44 mT, A_3(N) = 3.23 mT) was formed at the lower abundance. In contrast, the signal of $N_b^{\bullet}$ dominated the EPR spectra of samples M4–M6 upon visible-light exposure, and such behavior is typical for N-doped TiO_2 nanostructures assuming photoactivation of N_b^- species produced during synthesis.

The ability of photocatalysts dispersed in water or DMSO to generate non-persistent radical species was tested by spin trapping technique and reduction of semi-stable $ABTS^{\bullet+}$. The results of EPR spin trapping experiments in aqueous suspensions showed that paramagnetic species formed upon the exposure of dispersed g-C_3N_4/TiO_2 nanopowders sensitively reflect the initial weight ratio of annealed melamine/TiO_2, and the decrease in nitrogen-content in the synthesized photocatalysts M4–M6 is coupled with significant activity upon UV exposure and limited VIS-light activity. Despite the limitation of straightforward correlation between the relative integral intensity of paramagnetic species elucidated from the EPR spectra measured at 100 K and ROS generation in suspensions upon exposure, the visible-light activity of M4–M6 detected at 100 K and assigned to the formation $N_b^{\bullet}$ centers from N_b^- fits well the production of superoxide radical anion detected as the corresponding DMPO spin-adduct in aprotic DMSO solvent. With the aim of finding titania-based photocatalysts suitable for environmental application using solar-light exposure, nanopowder M4 prepared by the high-temperature treatment of melamine/TiO_2 wt. ratio of 1:3 revealed an adequate photoactivity in both spectral regions.

Acknowledgments: This study was financially supported by Scientific Grant Agency of the Slovak Republic (VEGA Project 1/0026/18) and by General Secretariat of Research and Technology of Greece (2D Photostructure project T1EDK-05545). The authors gratefully acknowledge Zuzana Ďurašová for technical assistance, Peter Segľa for the CHNS measurements and Zuzana Barbieriková for fruitful discussion and constructive comments.

Author Contributions: C.T., T.G. and I.P. prepared the samples. D.D., M.M. and V.B. performed the experiments, analyzed the data and wrote the paper.

Conflicts of Interest: The authors declare no conflict of interest.

References

1. Garcia-Segura, S.; Brillas, E. Applied photoelectrocatalysis on the degradation of organic pollutants in wastewaters. *J. Photochem. Photobiol. C* **2017**, *31*, 1–35. [CrossRef]
2. MiarAlipour, S.; Friedmann, D.; Scott, J.; Amal, R. TiO_2/porous adsorbents: Recent advances and novel applications. *J. Hazard. Mater.* **2018**, *341*, 404–423. [CrossRef] [PubMed]
3. Shayegan, Z.; Lee, C.S.; Haghighat, F. TiO_2 photocatalyst for removal of volatile organic compounds in gas phase—A review. *Chem. Eng. J.* **2018**, *334*, 2408–2439. [CrossRef]
4. Fujishima, A.; Zhang, X.; Tryk, D. TiO_2 photocatalysis and related surface phenomena. *Surf. Sci. Rep.* **2008**, *63*, 515–582. [CrossRef]

5. Diebold, U. The surface science of titanium dioxide. *Surf. Sci. Rep.* **2003**, *48*, 53–229. [CrossRef]
6. Carp, O.; Huisman, C.; Reller, A. Photoinduced reactivity of titanium dioxide. *Prog. Solid State Chem.* **2004**, *32*, 33–177. [CrossRef]
7. Schneider, J.; Matsuoka, M.; Takeuchi, M.; Zhang, J.; Horiuchi, Y.; Anpo, M.; Bahnemann, D.W. Understanding TiO_2 photocatalysis: Mechanisms and materials. *Chem. Rev.* **2014**, *114*, 9919–9986. [CrossRef] [PubMed]
8. Rahimi, N.; Pax, R.A.; Gray, E.M. Review of functional titanium oxides. I: TiO_2 and its modifications. *Prog. Solid State Chem.* **2016**, *44*, 86–105. [CrossRef]
9. Pelaez, M.; Nolan, N.; Pillai, S.; Seery, M.; Falaras, P.; Kontos, A.; Dunlop, P.; Hamilton, J.; Byrne, J.; O'Shea, K.; et al. A review on the visible light active titanium dioxide photocatalysts for environmental applications. *Appl. Catal. B* **2012**, *125*, 331–349. [CrossRef]
10. Etacheri, V.; Di Valentin, C.; Schneider, J.; Bahnemann, D.; Pillai, S.C. Visible-light activation of TiO_2 photocatalysts: Advances in theory and experiments. *J. Photochem. Photobiol. C* **2015**, *25*, 1–29. [CrossRef]
11. Sofianou, M.V.; Psycharis, V.; Boukos, N.; Vaimakis, T.; Yu, J.; Dillert, R.; Bahnemann, D.; Trapalis, C. Tuning the photocatalytic selectivity of TiO_2 anatase nanoplates by altering the exposed crystal facets content. *Appl. Catal. B* **2013**, *142–143*, 761–768. [CrossRef]
12. Kumar, S.G.; Rao, K.S.R.K. Comparison of modification strategies towards enhanced charge carrier separation and photocatalytic degradation activity of metal oxide semiconductors (TiO_2, WO_3 and ZnO). *Appl. Surf. Sci.* **2017**, *391*, 124–148. [CrossRef]
13. Borges, K.A.; Santos, L.M.; Paniago, R.M.; Barbosa Neto, N.M.; Schneider, J.; Bahnemann, D.W.; Patrocinio, A.O.T.; Machado, A.E.H. Characterization of a highly efficient N-doped TiO_2 photocatalyst prepared via factorial design. *New J. Chem.* **2016**, *40*, 7846–7855. [CrossRef]
14. Serpone, N.; Emeline, A.V. Semiconductor photocatalysis—Past, present, and future outlook. *J. Phys. Chem. Lett.* **2012**, *3*, 673–677. [CrossRef] [PubMed]
15. Emeline, A.V.; Kuznetsov, V.N.; Ryabchuk, V.K.; Serpone, N. On the way to the creation of next generation photoactive materials. *Environ. Sci. Pollut. Res.* **2012**, *19*, 3666–3675. [CrossRef] [PubMed]
16. Wen, J.; Xie, J.; Chen, X.; Li, X. A review on g-C_3N_4-based photocatalysts. *Appl. Surf. Sci.* **2017**, *391*, 72–123. [CrossRef]
17. Masih, D.; Ma, Y.; Rohani, S. Graphitic C_3N based noble-metal-free photocatalyst systems: A review. *Appl. Catal. B* **2017**, *206*, 556–588. [CrossRef]
18. Schwarzer, A.; Saplinova, T.; Kroke, E. Tri-s-triazines (s-heptazines)-from a "Mystery molecule" to industrially relevant carbon nitride materials. *Coord. Chem. Rev.* **2013**, *257*, 2032–2062. [CrossRef]
19. Dong, G.; Zhang, Y.; Pan, Q.; Qiu, J. A fantastic graphitic carbon nitride (g-C_3N_4) material: Electronic structure, photocatalytic and photoelectronic properties. *J. Photochem. Photobiol. C* **2014**, *20*, 33–50. [CrossRef]
20. Zhou, L.; Wang, L.; Zhang, J.; Lei, J.; Liu, Y. The preparation, and applications of g-C_3N_4/TiO_2 heterojunction catalysts—A review. *Res. Chem. Intermed.* **2017**, *43*, 2081–2101. [CrossRef]
21. Lu, X.; Wang, Q.; Cui, D. Preparation and photocatalytic properties of g-C_3N_4/TiO_2 hybrid composite. *J. Mater. Sci. Technol.* **2010**, *26*, 925–930. [CrossRef]
22. Sridharan, K.; Jang, E.; Park, T.J. Novel visible light active graphitic C_3N_4-TiO_2 composite photocatalyst: Synergistic synthesis, growth and photocatalytic treatment of hazardous pollutants. *Appl. Catal. B* **2013**, *142–143*, 718–728. [CrossRef]
23. Papailias, I.; Todorova, N.; Giannakopoulou, T.; Yu, J.; Dimotikali, D.; Trapalis, C. Photocatalytic activity of modified g-C_3N_4/TiO_2 nanocomposites for NO_x removal. *Catal. Today* **2017**, *280*, 37–44. [CrossRef]
24. Giannakopoulou, T.; Papailias, I.; Todorova, N.; Boukos, N.; Liu, Y.; Yu, J.; Trapalis, C. Tailoring the energy band gap and edges' potentials of g-C_3N_4/TiO_2 composite photocatalysts for NO_x removal. *Chem. Eng. J.* **2017**, *310*, 571–580. [CrossRef]
25. Dvoranová, D.; Barbieriková, Z.; Brezová, V. Radical intermediates in photoinduced reactions on TiO_2 (An EPR spin trapping study). *Molecules* **2014**, *19*, 17279–17304. [CrossRef] [PubMed]
26. Barbieriková, Z.; Dvoranová, D.; Sofianou, M.V.; Trapalis, C.; Brezová, V. UV-induced reactions of Mg^{2+}-doped anatase nanocrystals with exposed {001} facets: An EPR study. *J. Catal.* **2015**, *331*, 39–48. [CrossRef]
27. Pližingrová, E.; Klementová, M.; Bezdička, P.; Boháček, J.; Barbieriková, Z.; Dvoranová, D.; Mazúr, M.; Krýsa, J.; Šubrt, J.; Brezová, V. 2D-titanium dioxide nanosheets modified with Nd, Ag and Au: Preparation, characterization and photocatalytic activity. *Catal. Today* **2017**, *281*, 165–180. [CrossRef]

28. Hurum, D.C.; Gray, K.A.; Rajh, T.; Thurnauer, M.C. Recombination pathways in the Degussa P25 formulation of TiO_2: Surface versus lattice mechanisms. *J. Phys. Chem. B* **2005**, *109*, 977–980. [CrossRef] [PubMed]
29. Hurum, D.C.; Agrios, A.G.; Gray, K.A.; Rajh, T.; Thurnauer, M.C. Explaining the enhanced photocatalytic activity of Degussa P25 mixed-phase TiO_2 using EPR. *J. Phys. Chem. B* **2003**, *107*, 4545–4549. [CrossRef]
30. Ho, W.; Zhang, Z.; Xu, M.; Zhang, X.; Wang, X.; Huang, Y. Enhanced visible-light-driven photocatalytic removal of NO: Effect on layer distortion on g-C_3N_4 by H_2 heating. *Appl. Catal. B* **2015**, *179*, 106–112. [CrossRef]
31. Serwicka, E. Localization of conduction band electrons in polycrystalline TiO_2 studied by ESR. *Z. Naturforsch. A Phys. Sci.* **1981**, *36*, 226–2325.
32. Chiesa, M.; Paganini, M.C.; Livraghi, S.; Giamello, E. Charge trapping in TiO_2 polymorphs as seen by Electron Paramagnetic Resonance spectroscopy. *Phys. Chem. Chem. Phys.* **2013**, *15*, 9435–9447. [CrossRef] [PubMed]
33. Weil, J.A.; Bolton, J.R. *Electron Paramagnetic Resonance. Elementary Theory and Practical Applications*, 2nd ed.; John Wiley & Sons: Hoboken, NJ, USA, 2007; p. 583. ISBN 978-0-471-75496-1.
34. Livraghi, S.; Rolando, M.; Maurelli, S.; Chiesa, M.; Paganini, M.C.; Giamello, E. Nature of reduced states in titanium dioxide as monitored by Electron Paramagnetic Resonance. II: Rutile and brookite cases. *J. Phys. Chem. C* **2014**, *118*, 22141–22148. [CrossRef]
35. Zhang, Z.; Long, J.; Xie, X.; Lin, H.; Zhou, Y.; Yuan, R.; Dai, W.; Ding, Z.; Wang, X.; Fu, X. Probing the electronic structure and photoactivation process of nitrogen-doped TiO_2 using DRS, PL, and EPR. *ChemPhysChem* **2012**, *13*, 1542–1550. [CrossRef] [PubMed]
36. Livraghi, S.; Chiesa, M.; Paganini, M.; Giamello, E. On the nature of reduced states in titanium dioxide as monitored by Electron Paramagnetic Resonance. I: The anatase case. *J. Phys. Chem. C* **2011**, *115*, 25413–25421. [CrossRef]
37. Bianchi, C.L.; Cappelletti, G.; Ardizzone, S.; Gialanella, S.; Naldoni, A.; Oliva, C.; Pirola, C. N-doped TiO_2 from $TiCl_3$ for photodegradation of air pollutants. *Catal. Today* **2009**, *144*, 31–36. [CrossRef]
38. Di Valentin, C.; Finazzi, E.; Pacchioni, G.; Selloni, A.; Livraghi, S.; Paganini, M.C.; Giamello, E. N-doped TiO_2: Theory and experiment. *Chem. Phys.* **2007**, *339*, 44–56. [CrossRef]
39. Di Valentin, C.; Pacchioni, G.; Selloni, A.; Livraghi, S.; Giamello, E. Characterization of paramagnetic species in N-doped TiO_2 powders by EPR spectroscopy and DFT calculations. *J. Phys. Chem. B* **2005**, *109*, 11414–11419. [CrossRef] [PubMed]
40. Livraghi, S.; Paganini, M.C.; Giamello, E.; Selloni, A.; Di Valentin, C.; Pacchioni, G. Origin of photoactivity of nitrogen-doped titanium dioxide under visible light. *J. Am. Chem. Soc.* **2006**, *128*, 15666–15671. [CrossRef] [PubMed]
41. Fittipaldi, M.; Gatteschi, D.; Fornasiero, P. The power of EPR techniques in revealing active sites in heterogeneous photocatalysis: The case of anion doped TiO_2. *Catal. Today* **2013**, *206*, 2–11. [CrossRef]
42. Darienzo, M.; Siedl, N.; Sternig, A.; Scotti, R.; Morazzoni, F.; Bernardi, J.; Diwald, O. Solar light and dopant-induced recombination effects: Photoactive nitrogen in TiO_2 as a case study. *J. Phys. Chem. C* **2010**, *114*, 18067–18072. [CrossRef]
43. D'Arienzo, M.; Scotti, R.; Wahba, L.; Battocchio, C.; Bemporad, E.; Nale, A.; Morazzoni, F. Hydrothermal N-doped TiO_2: Explaining photocatalytic properties by electronic and magnetic identification of N active sites. *Appl. Catal. B* **2009**, *93*, 149–155. [CrossRef]
44. Di Valentin, C.; Pacchioni, G.; Selloni, A. Origin of the different photoactivity of N-doped anatase and rutile TiO_2. *Phys. Rev. B Condens. Matter Mater. Phys.* **2004**, *70*, 085116. [CrossRef]
45. Moustakas, N.G.; Kontos, A.G.; Likodimos, V.; Katsaros, F.; Boukos, N.; Tsoutsou, D.; Dimoulas, A.; Romanos, G.E.; Dionysiou, D.D.; Falaras, P. Inorganic-organic core-shell titania nanoparticles for efficient visible light activated photocatalysis. *Appl. Catal. B* **2013**, *130–131*, 14–24. [CrossRef]
46. Nosaka, Y.; Nosaka, A.Y. Generation and detection of reactive oxygen species in photocatalysis. *Chem. Rev.* **2017**, *117*, 11302–11336. [CrossRef] [PubMed]
47. Lipovsky, A.; Levitski, L.; Tzitrinovich, Z.; Gedanken, A.; Lubart, R. The different behavior of rutile and anatase nanoparticles in forming oxy radicals upon illumination with visible light: An EPR study. *Photochem. Photobiol.* **2012**, *88*, 14–20. [CrossRef] [PubMed]

48. Nosaka, Y.; Komori, S.; Yawata, K.; Hirakawa, T.; Nosaka, A. Photocatalytic $^{\bullet}$OH radical formation in TiO_2 aqueous suspension studied by several detection methods. *Phys. Chem. Chem. Phys.* **2003**, *5*, 4731–4735. [CrossRef]
49. Wang, Z.; Ma, W.; Chen, C.; Ji, H.; Zhao, J. Probing paramagnetic species in titania-based heterogeneous photocatalysis by electron spin resonance (ESR) spectroscopy—A mini review. *Chem. Eng. J.* **2011**, *170*, 353–362. [CrossRef]
50. Buettner, G.R. Spin trapping: ESR parameters of spin adducts. *Free Radic. Biol. Med.* **1987**, *3*, 259–303. [CrossRef]
51. Brezová, V.; Dvoranová, D.; Staško, A. Characterization of titanium dioxide photoactivity following the formation of radicals by EPR spectroscopy. *Res. Chem. Intermed.* **2007**, *33*, 251–268. [CrossRef]
52. Hayyan, M.; Hashim, M.A.; Alnashef, I.M. Superoxide ion: Generation and chemical implications. *Chem. Rev.* **2016**, *116*, 3029–3085. [CrossRef] [PubMed]
53. Zhao, H.; Joseph, J.; Zhang, H.; Karoui, H.; Kalyanaraman, B. Synthesis and biochemical applications of a solid cyclic nitrone spin trap: A relatively superior trap for detecting superoxide anions and glutathiyl radicals. *Free Radic. Biol. Med.* **2001**, *31*, 599–606. [CrossRef]
54. Brezová, V.; Gabčová, S.; Dvoranová, D.; Staško, A. Reactive oxygen species produced upon photoexcitation of sunscreens containing titanium dioxide (an EPR study). *J. Photochem. Photobiol. B* **2005**, *79*, 121–134. [CrossRef] [PubMed]
55. Barbieriková, Z.; Pližingrová, E.; Motlochová, M.; Bezdička, P.; Boháček, J.; Dvoranová, D.; Mazúr, M.; Kupčík, J.; Jirkovský, J.; Šubrt, J.; et al. N-doped titanium dioxide nanosheets: Preparation, characterization and UV/visible-light activity. *Appl. Catal. B* **2017**. submitted.
56. Brezová, V.; Barbieriková, Z.; Dvoranová, D.; Staško, A. UVA-induced processes in the aqueous titanium dioxide suspensions containing nitrite (An EPR spin trapping study). *J. Adv. Oxid. Technol.* **2016**, *19*, 290–301. [CrossRef]
57. Re, R.; Pellegrini, N.; Proteggente, A.; Pannala, A.; Yang, M.; Rice-Evans, C. Antioxidant activity applying an improved ABTS radical cation decolorization assay. *Free Radic. Biol. Med.* **1999**, *26*, 1231–1237. [CrossRef]
58. Stoll, S.; Schweiger, A. EasySpin, a comprehensive software package for spectral simulation and analysis in EPR. *J. Magn. Reson.* **2006**, *178*, 42–55. [CrossRef] [PubMed]
59. Duling, D.R. Simulation of multiple isotropic spin-trap EPR spectra. *J. Magn. Reson. B* **1994**, *104*, 105–110. [CrossRef] [PubMed]